In-line femtosecond common-path interferometer in reflection mode

J. Chandezon,[1,2] J.-M. Rampnoux,[2] S. Dilhaire,[2] B. Audoin,[1] and Y. Guillet[1,*]

[1] *Univ. Bordeaux, I2M, UMR 5295, F-33405 Talence, France*
[2] *Univ. Bordeaux, LOMA, UMR 5798, F-33405 Talence, France*

[*] *yannick.guillet@u-bordeaux.fr*

Abstract: An innovative method to perform femtosecond time-resolved interferometry in reflection mode is proposed. The experiment consists in the combined use of a pump-probe setup and of a fully passive in-line femtosecond common-path interferometer. The originality of this interferometer relies on the use of a single birefringent crystal first to generate a pair of phase-locked pulses and second to recombine them to interfere. As predicted by analytical modeling, this interferometer measures the temporal derivative of the ultrafast changes of the complex optical reflection coefficient of the sample. Working conditions are illustrated through picosecond opto-acoustic experiments on a thin film.

OCIS codes: (300.6500) Spectroscopy, time-resolved; (120.3180) Interferometry; (320.5390) Picosecond phenomena.

References and links

1. J.-M. Halbout and C. L. Tang, "Femtosecond interferometry for nonlinear optics," Appl. Phys. Lett. **40**, 765–767 (1982).
2. D. Cotter, C. N. Ironside, B. J. Ainslie, and H. P. Girdlestone, "Picosecond pump-probe interferometric measurement of optical nonlinearity in semiconductor-doped fibers," Opt. Lett. **14**, 317–319 (1989).
3. N. Finlayson, W. C. Banyai, C. T. Seaton, G. I. Stegeman, M. O'Neill, T. J. Cullen, and C. N. Ironside, "Optical nonlinearities in CdS_xSe_{1-x}-doped glass waveguides," J. Opt. Soc. Am. B **6**, 675–684 (1989).
4. E. Tokunaga, A. Terasaki, and T. Kobayashi, "Frequency-domain interferometer for femtosecond time-resolved phase spectroscopy," Opt. Lett. **17**, 1131–1133 (1992).
5. P. Audebert, Ph. Daguzan, A. Dos Santos, J. C. Gauthier, J. P. Geindre, S. Guizard, G. Hamoniaux, K. Krastev, P. Martin, G. Petite, and A. Antonetti, "Space-time observation of an electron gas in SiO_2," Phys. Rev. Lett. **73**, 1990–1993 (1994).
6. V. V. Temnov, K. Sokolowski-Tinten, P. Zhou, A. El-Khamhawy, and D. von der Linde, "Multiphoton ionization in dielectrics: Comparison of circular and linear polarization," Phys. Rev. Lett. **97**, 237403 (2006).
7. C. Sarpe, J. Köhler, T. Winkler, M. Wollenhaupt, and T. Baumert, "Real-time observation of transient electron density in water irradiated with tailored femtosecond laser pulses," New J. Phys. **14**, 075021 (2012).
8. M. J. LaGasse, D. Liu-Wong, J. G. Fujimoto, and H. A. Haus, "Ultrafast switching with a single-fiber interferometer," Opt. Lett. **14**, 311–313 (1989).
9. B. Perrin, B. Bonello, J.-C. Jeannet, and E. Romatet, "Interferometric detection of hypersound waves in modulated structures," Prog. Nat. Sci. **S6**, 444–448 (1996).
10. D. H. Hurley and O. B. Wright, "Detection of ultrafast phenomena by use of a modified sagnac interferometer," Opt. Lett. **24**, 1305–1307 (1999).
11. F. Decremps, L. Belliard, B. Perrin, and M. Gauthier "Sound Velocity and Absorption Measurements under High Pressure Using Picosecond Ultrasonics in a Diamond Anvil Cell: Application to the Stability Study of AlPdMn," Phys. Rev. Lett. **100**, 035502 (2008).
12. J.-Y. Duquesne, and B. Perrin, "Ultrasonic attenuation in a quasicrystal studied by picosecond acoustics as a function of temperature and frequency," Phys. Rev. B **68**, 134205 (2003).

13. R. Evans, A. D. Badger, F. Falliès, M. Mahdieh, T. A. Hall, P. Audebert, J.-P. Geindre, J.-C. Gauthier, A. Mysyrowicz, G. Grillon, and A. Antonetti, "Time- and space-resolved optical probing of femtosecond-laser-driven shock waves in aluminum," Phys. Rev. Lett. **77**, 3359–3362 (1996).
14. K. Misawa and T. Kobayashi, "Femtosecond sagnac interferometer for phase spectroscopy," Opt. Lett. **20**, 1550–1552 (1995).
15. M. Nikoonahad, S. Lee, and H. Wang, "Picosecond photoacoustics using common-path interferometry," Appl. Phys. Lett. **76**, 514–516 (2000).
16. M. A. van Dijk, M. Lippitz, and M. Orrit, "Detection of acoustic oscillations of single gold nanospheres by time-resolved interferometry," Phys. Rev. Lett. **95**, 267406 (2005).
17. M. A. van Dijk, M. Lippitz, D. Stolwijk, and M. Orrit, "A common-path interferometer for time-resolved and shot-noise-limited detection of single nanoparticles," Opt. Express **15**, 2273–2287 (2007).
18. S. Dobner, P. Groß, and C. Fallnich, "In-line interferometric femtosecond stimulated raman scattering spectroscopy," J. Chem. Phys. **138**, 244201 (2013).
19. G. A. Antonelli, B. Perrin, B. C. Daly and D. G. Cahill, "Characterization of Mechanical and Thermal Properties Using Ultrafast Optical Metrology," MRS Bull. **31**, 607–613 (2006).
20. J. P. Geindre, A. Mysyrowicz, A. Dos Santos, P. Audebert, A. Rousse, G. Hamoniaux, A. Antonetti, F. Fallis, and J. C. Gauthier, "Frequency-domain interferometer for measuring the phase and amplitude of a femtosecond pulse probing a laser-produced plasma," Opt. Lett. **19**, 1997–1999 (1994).
21. C. Thomsen, T. H. Grahn, H. J. Maris, and J. Tauc, "Surface generation and detection of phonons by picosecond light pulses," Phys. Rev. B **34**, 4129–4138 (1986).
22. H. N. Lin, R. J. Stoner, H. J. Maris, and J. Tauc, "Phonon attenuation and velocity measurements in transparent materials by picosecond acoustic interferometry," J. Appl. Phys. **69**, 3816–3822 (1991).
23. N. Deguil, E. Mottay, F. Salin, P. Legros, and D. Choquet, "Novel diode-pumped infrared tunable laser system for multi-photon microscopy," Microsc. Res. Tech. **63**, 23–26 (2004).
24. A. Bartels, F. Hudert, C. Janke, T. Dekorsy, and K. Kohler, "Femtosecond time-resolved optical pump-probe spectroscopy at kilohertz-scan-rates over nanosecond-time-delays without mechanical delay line," Appl. Phys. Lett. **88**, 041117 (2006).
25. A. Abbas, Y. Guillet, J.-M. Rampnoux, P. Rigail, E. Mottay, B. Audoin, and S. Dilhaire, "Picosecond time resolved opto-acoustic imaging with 48 mhz frequency resolution," Opt. Express **22**, 7831–7843 (2014).
26. S. Dilhaire, J. M. Rampnoux, W. Claeys, and C. Rossignol, "Optical heterodyne sampling device," Patent WO2006FR02384 20061020, FR20050010776 20051021 (2005).
27. G. Ghosh, "Dispersion-equation coefficients for the refractive index and birefringence of calcite and quartz crystals," Opt. Commun. **163**, 95–102 (1999).
28. O. Schubert, M. Eisele, V. Crozatier, N. Forget, D. Kaplan, and R. Huber, "Rapid-scan acousto-optical delay line with 34 khz scan rate and 15 as precision," Opt. Lett. **38**, 2907–2910 (2013).
29. D. Brida, C. Manzoni, and G. Cerullo, "Phase-locked pulses for two-dimensional spectroscopy by a birefringent delay line," Opt. Lett. **37**, 3027–3029 (2012).
30. J. Réhault, M. Maiuri, C. Manzoni, D. Brida, J. Helbing, and G. Cerullo, "2D IR spectroscopy with phase-locked pulse pairs from a birefringent delay line," Opt. Express **22**, 9063–9072 (2014).
31. R. C. Jones, "A new calculus for the treatment of optical systems," J. Opt. Soc. Am. **31**, 488–493 (1941).
32. J. E. Rothenberg, "Observation of the transient expansion of heated surfaces by picosecond photothermal deflection spectroscopy," Opt. Lett. **13**, 713–715 (1988).
33. O. B. Wright, and K. Kawashima, "Coherent phonon detection from ultrafast surface vibrations," Phys. Rev. Lett. **69**, 1668-1671 (1992).
34. H. Yamazaki, O. Matsuda, and O. B. Wright, "Surface phonon imaging through the photoelastic effect," Phys. stat. sol. (c) **1**, 2991–2994 (2004).
35. N. Chigarev, C. Rossignol, and B.Audoin, "Surface displacement measured by beam distortion detection technique: Application to picosecond ultrasonics," Rev. Sci. Instrum. **77**, 114901 (2006).
36. R. Salenbien, R. Cote, J. Goossens, P. Limaye, R. Labie, C. Glorieux, "Laser-based surface acoustic wave dispersion spectroscopy for extraction of thicknesses, depth, and elastic parameters of a subsurface layer: Feasibility study on intermetallic layer structure in integrated circuit solder joint," J. Appl. Phys. **109**, 093104 (2011).
37. J. Higuet, T. Valier - Brasier, T. Dehoux, and B. Audoin, "Beam distortion detection and deflectometry measurements of gigahertz surface acoustic waves," Rev. Sci. Instrum. **82**, 114905 (2011).
38. B. Perrin, C. Rossignol, B. Bonello, and J.-C. Jeannet, "Interferometric detection in picosecond ultrasonics," Physica B **263-264**, 571–573 (1999).
39. Y. Sugawara, O. B. Wright, O. Matsuda, and V. E. Gusev, "Spatiotemporal mapping of surface acoustic waves in isotropic and anisotropic materials," Ultrasonics **40**, 55–59 (2002).
40. O. Matsuda, M. Tomoda, T. Tachizaki, S. Koiwa, A. Ono, K. Aoki, R. P. Beardsley, and O. B. Wright, "Ultrafast ellipsometric interferometry for direct detection of coherent phonon strain pulse profiles," J. Opt. Soc. Am. B **30**, 1911–1921 (2013).
41. R. W. Schoenlein, W. Z. Lin, J. G. Fujimoto, and G. L. Eesley, "Femtosecond studies of nonequilibrium electronic processes in metals," Phys. Rev. Lett. **58**, 1680–1683 (1987).
42. V. E. Gusev and A. A. Karabutov. *Laser Optoacoustics* (AIP, New York, 1993).

1. Introduction

Femtosecond time-resolved interferometry has been proposed in 1982 by Halbout and Tang [1]. This technique has proved to be a powerful tool in the broad field of laser-matter interaction since it is able to resolve the laser-induced transient modification of the complex refractive index of a sample. For instance, applications have been developed in nonlinear optics [1–4], laser-dielectric interaction [5–7], THz optical switching [8] and THz acoustics [9, 10].

Double-path interferometers have been the first setups used in femtosecond time-resolved interferometry, notably the Mach-Zehnder [1–3, 6, 9] and Michelson [11] interferometers, where the position of the reference mirror is controlled with an active feedback loop. On the other hand, common-path interferometers have emerged in the 90's [8]. Two widespread ways to generate the reference and probe pulses consist either in inserting a beamsplitter before the sample [4, 5, 13] or in using a Sagnac interferometer [10, 12, 14, 15]. Depending on the temporal delay between the reference and probe pulses in the common-path interferometer, either the perturbation of the complex refractive index [4–8] or its temporal derivative [7] is measured. Ten years ago, van Dijk et al. [16, 17] have proposed an alternative approach. The beamsplitter used in a Sagnac interferometer to create the reference and probe beams has been replaced by a birefringent crystal which generates a pair of phase-locked pulses with orthogonal polarization. The temporal delay between the reference and probe pulses is then imposed by the birefringence of the crystal and by its thickness. This in-line interferometer is extremely stable and easy to align, leading to a high fringe contrast. Following this pioneering work, other groups have developed similar interferometers [7, 18]. Sarpe et al. have proposed to use additional birefringent crystals after the sample to reduce the delay between reference and probe pulses down to 200 fs before recording interferences in the spectral domain [7]. However, all the aforementioned common-path interferometers employing birefringent crystals have only been used in a transmission mode. Furthermore, two birefringent crystals are used: One temporally separates the reference and probe pulses whereas the second recombines them. An active control of the temperature of both crystals is thus required to ensure stability of the interferometer [17].

In this article, we present a fully passive in-line femtosecond time-resolved common-path interferometer in reflection mode where a single birefringent crystal is used. This crystal first temporally separates the reference and probe pulses and then recombines them to get interferences. The reflection mode is ideally suited to study opaque samples [9, 10, 19, 20] or to perform time-resolved Brillouin spectroscopy [21, 22]. The article is organized as follows. In Section 2, we describe the interferometric pump-probe setup and we present the principle of operation of the interferometer. In Section 3 the Jones formalism is used to show how the pump-induced modification of the real and imaginary parts of the complex reflection coefficient of the sample can be inferred independently. In Section 4, we illustrate the performance of the interferometer through picosecond opto-acoustic measurements on a thin film. The volume strain and the surface displacement induced by the longitudinal acoustic waves propagating back and forth in a thin film are detected with the common-path interferometer.

2. Interferometric femtosecond pump-probe setup

Figure 1 shows the interferometric femtosecond pump-probe setup. The laser source is a compact dual-oscillator (t-Pulse Duo, Amplitudes Systèmes, France) [23]. The pump-probe setup relies on the asynchronous optical sampling technique (ASOPS) where the pump-probe delay is generated by using two pulsed lasers at slightly different repetition rates [24, 25]. The probe and pump lasers deliver 330 fs pulses at 1027 nm and 430 fs pulses at 1040 nm, respectively.

The beating frequency $\Delta f = 500\,\mathrm{Hz}$ between the probe laser repetition frequency $f = 48\,\mathrm{MHz}$ and the pump laser repetition frequency $f + \Delta f$ is generated by a frequency synthesizer and is stabilized using an active feedback loop [26]. The resulting temporal resolution in pump-probe measurements is close to 1 ps over a 20 ns temporal window [25].

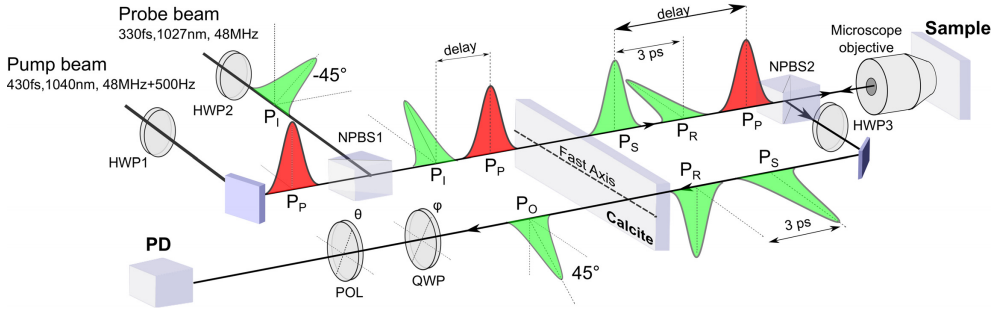

Fig. 1. Scheme of the in-line femtosecond common-path interferometer coupled to an ASOPS pump-probe experiment. HWP1 to HWP3: half-wave plates, NPBS1 and NPBS2: non-polarizing beam-splitters, QWP: quarter-wave plate, Pol: polarizer, P_P: pump pulse, P_I: pulse at the input of the interferometer, P_O: pulse at the output of the interferometer, P_S: probe pulse, P_R: reference pulse. The time zero is defined as the overlap between the pump and the probe pulses. Angles are given relatively to the fast optical axis of the birefringent calcite crystal. See text for a detailed description.

The in-line femtosecond common-path interferometer in reflection mode is inserted in the pump-probe setup. The optical element playing a central role in this interferometer is the birefringent crystal [17]. All angle values used hereinafter are given relatively to the fast optical axis of the birefringent crystal. The linear polarization of the pulse P_I incident on the crystal is oriented at -45 degrees by a half-wave plate (HWP2). Due to different ordinary and extraordinary refractive indices of the crystal, two time-delayed pulses - the reference pulse P_R and the probe pulse P_S - emerge at the crystal output and are linearly polarized along its fast and slow optical axes, respectively. A 5 mm-thick calcite crystal have been used, leading to a 3 ps-temporal delay between the two generated pulses [27]. A $\times 20$ microscope objective focuses the pulses P_R and P_S on the sample and collects them after reflection. The strength of this interferometer is to use a single birefringent crystal first to temporally separate the pulses P_R and P_S before they probe the sample and second to recombine them after their reflection on the sample to interfere. Before passing through the same calcite crystal, the backward optical path is separated from the forward optical path by the non-polarizing beamsplitter NPBS2. After the half-wave plate HWP3 oriented at 45 degrees, the pulse P_R and P_S have their linear polarization swapped. Thus, after the backward passage inside the calcite crystal, the pulses P_R and P_S are temporally overlapped. These pulses are sent into an analyzer composed of a quarter-wave plate (QWP, angle ϕ) and a polarizer (Pol, angle θ). The pulse at the output of the polarizer results from the interference between the electric fields of pulses P_R and P_S. An amplified silicon differential photodiode PD (Thorlabs, model PDB450C) directly measures the intensity of the interference state at the output of the polarizer.

Let us remind that before the first passage through the calcite crystal, the incident pulse is polarized at -45 degrees. The generated reference and probe electric fields after the second passage in the crystal thus have same amplitude, and interferences with a maximum contrast are ensured. In the absence of excitation, the temporal recombination of the pulses P_R and P_S leads to a unique pulse P_O linearly polarized at 45 degrees. Now a detailed description is given on how the pump-induced perturbation to the interference state is detected. In the following,

the time zero is defined as the overlap between the pump and the probe pulses. The half-wave plate HWP1 aligns the linear polarization of the pump along the fast or the slow optical axis of the crystal to get a single pump pulse at the crystal output. In the following, the polarization of the pump pulse has been arbitrarily chosen along the slow axis of the crystal. The pump pulse passes through the same microscope objective as the pulses P_R and P_S and is focused on the sample. The perturbation of the optical properties of the sample induced by the absorption of the pump pulse modifies both amplitude and phase of the electric fields of both reflected reference and probe pulses. Since pulses P_R and P_S are 3 ps time-delayed at the sample position, the perturbation of the electric field of the two pulses P_R and P_S are slightly different. Therefore, after the second passage inside the calcite crystal, the polarization of the recombined pulse P_O becomes elliptical or is still linear but with a rotated angle [17]. For pump-probe delays higher than 3 ps, the interference state at the output of the analyzer thus carries information on the temporal derivative of the perturbed optical reflection coefficient. As it will be detailed in Section 3, depending on the angle of the quarter-wave plate and of the polarizer, the derivative of either the real or the imaginary parts of the perturbed optical reflection coefficient can be measured independently. In the spectral domain, this time-resolved interferometer behaves as a band-pass filter. The lower cutoff frequency comes from the sensitivity to the derivative of the perturbation and the 3-ps temporal delay between the reference and probe pulses imposes a 150 GHz-higher cutoff frequency. However, this upper limit could be pushed towards the THz by using a thinner crystal, an acousto-optical delay line [28] or a combination of several birefringent crystals [7, 29, 30].

Compared with the Sagnac interferometer [10,12], the spatial splitting of a single probe pulse into two pulses has been replaced by the in-line generation of a pair of phase-locked pulses from a birefringent delay line. This original configuration allows a straightforward optical alignment since reference and probe arms are spatially overlapped all along the optical path. Furthermore, compared with the interferometer developed by van Dijk *et al.* [17], the configuration we propose here is strongly simplified since we use one birefringent crystal only. In the van Dijk's configuration, an active control of the temperature of the birefringent crystals is required to ensure an optimal stability of the interferometer. In the reflection mode presented here, this active control is no longer needed, the interferometer then being entirely passive.

3. Modeling of the interferometer sensitivity

Let θ and ϕ denote the angles of the polarizer (Pol) and the quarter-wave plate (QWP), respectively. The Jones formalism [31] is well suited to predict in the (θ,ϕ) space the optimum working point of this polarization based interferometer. This matrix approach has been used by van Dijk *et al*. for the transmission mode of their interferometer [17]. Extension of the modeling to the reflection mode is given hereinafter.

The electric field $\mathbf{E_{in}}$ (amplitude E_0) of the pulse P_I incident on the calcite crystal is linearly polarized at -45 degrees, $\mathbf{E_{in}} = E_0/\sqrt{2}(1,-1)$. All optical elements are modeled by their representative Jones matrices. The electric field of the pulse at the output of the polarizer results from the multiplication of the equivalent Jones matrix representative of the whole optical elements by the incident electric field $\mathbf{E_{in}}$. Compared with the van Dijk's configuration, two Jones matrices have to be added in the calculation. The first one accounts for the reflection on the sample and the second is associated to the half-wave plate HWP3 oriented at 45 degrees. As mentioned in the previous section, since pulses P_R and P_S are 3 ps-time delayed, the perturbations of the optical reflection coefficient of the sample detected by these two pulses for a given pump-probe delay τ are slightly different. The relative perturbation of the magnitude of an electric field reflected at a pump-probe delay τ is denoted $\xi(\tau)$. The perturbed reflected reference and probe electric fields are thus equal to $E_R(\tau) = -r_0E_0[1+\xi(\tau)]$ and

$E_S(\tau) = r_0 E_0[1+\xi(\tau+t_0)]$, respectively. r_0 denotes the equilibrium reflection coefficient and $t_0 = 3$ps is the temporal delay between pulses P_R and P_S. For a given pump-probe delay τ, two unknown complex valued parameters have to be determined, namely $\xi(\tau)$ and $\xi(\tau+t_0)$. However, by choosing a working point of the interferometer close to a dark fringe, it is possible to assess directly $\Delta\xi(\tau) = \xi(\tau+t_0) - \xi(\tau)$ [17]. The intensity I at the output of the analyzer thus depends on θ, ϕ and $\Delta\xi(\tau)$ only.

When the pump is switched off, i.e. for $\Delta\xi(\tau) = 0$, the pulse P_O is linearly polarized at 45 degrees. In this specific case, a straightforward calculation shows that the intensity at the output of the polarizer is equal to $I[\theta,\phi,\Delta\xi(\tau)=0] = I_0[1+\cos(2\theta-2\phi)\sin 2\phi]/2$, where I_0 stands for the intensity at the bright fringe. Figure 2(a) shows the evolution of $I[\theta,\phi,\Delta\xi(\tau)=0]$ in the (θ,ϕ) space. For θ and ϕ ranging in the interval $[0,\pi]$, dark fringes are located at $(3\pi/4,\pi/4)$ and $(3\pi/4,3\pi/4)$ and bright fringes are located at $(\pi/4,\pi/4)$ and $(\pi/4,3\pi/4)$.

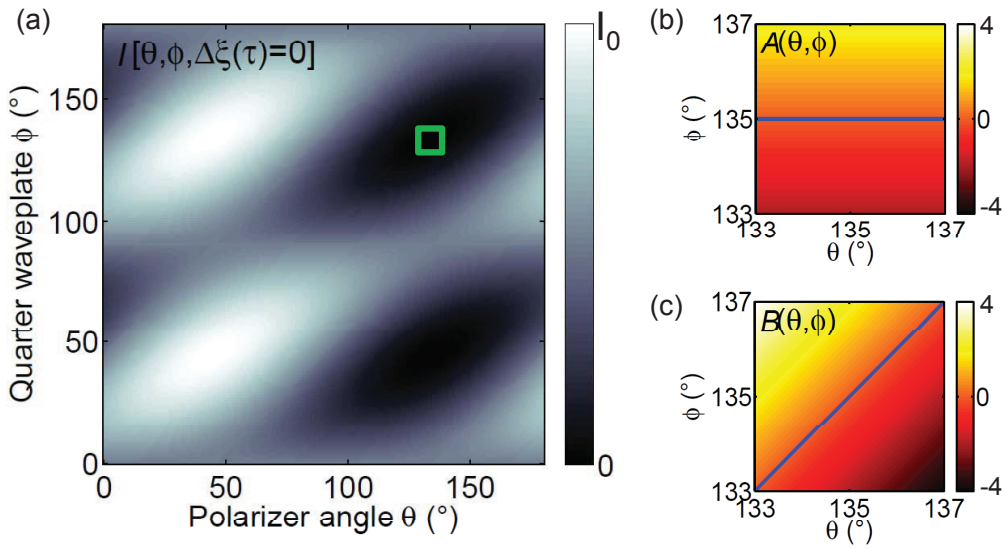

Fig. 2. (a) Evolution in the (θ,ϕ) space of the intensity at the output of the polarizer when the pump is switched off. (b) and (c) When the pump is switched on, evolution close to the dark fringe (green square in (a)) of functions $A(\theta,\phi)$ and $B(\theta,\phi)$ with respect to the polarizer angle θ and the quarter-wave plate angle ϕ. The values in the color bars are in degrees. The continuous blue lines show the domains where A and B are equal to zero.

When the pump is switched on, the transient perturbation ΔI of the intensity I measured by the detector is defined as:

$$\Delta I[\theta,\phi,\Delta\xi(\tau)] = I[\theta,\phi,\Delta\xi(\tau)] - I[\theta,\phi,\Delta\xi(\tau)=0] \quad . \tag{1}$$

Inferring independently the real part $\mathrm{Re}(\Delta\xi(\tau))$ and the imaginary part $\mathrm{Im}(\Delta\xi(\tau))$ of the perturbation is *a priori* not straightforward. For an arbitrary choice of θ and ϕ, the relative variation $\Delta I/I_0$ carries information on $\mathrm{Re}[\Delta\xi(\tau)]$ and $\mathrm{Im}[\Delta\xi(\tau)]$ at the same time. As mentioned above, transient reflectivity measurements are performed close to a dark fringe to directly assess $\Delta\xi(\tau)$ [17]. We discuss in the following the sensitivity to either the real part or the imaginary part of $\Delta\xi$ close to the dark fringe located at $(\theta,\phi) = (3\pi/4, 3\pi/4)$ (green square in Fig. 2 (a)). Note that owing to a $\pi/2$-periodicity of $I[\theta,\phi,\Delta\xi(\tau)=0]$ with respect to ϕ, the analysis would be similar close to $(\theta,\phi) = (3\pi/4,\pi/4)$. $\Delta I/I_0$ has been calculated at the first order in $\delta\theta$ and $\delta\phi$, where $\theta = 3\pi/4+\delta\theta$ and $\phi = 3\pi/4+\delta\phi$:

$$\frac{\Delta I}{I_0} = A(\theta,\phi)\mathrm{Re}[\Delta\xi(\tau)] + B(\theta,\phi)\mathrm{Im}[\Delta\xi(\tau)] \qquad , \tag{2}$$

where $A(\theta,\phi) = \delta\phi$ and $B(\theta,\phi) = \delta\theta - \delta\phi$. Figure 2(b) shows the evolution of $A(\theta,\phi)$ (top) and $B(\theta,\phi)$ (bottom) with respect to θ and ϕ. Two specific domains in the (θ,ϕ) space can be identified from Eq. 2 and are shown in Fig. 2(b) by the continuous blue lines. These lines correspond to the contour where functions A (top panel) or B (bottom panel) are equal to zero. For $\delta\phi = 0$ and $\delta\theta \neq 0$, ΔI is proportional to $\mathrm{Im}[\Delta\xi(\tau)]$ only, while for $\delta\theta = \delta\phi$ and $\delta\theta \neq 0$, $\Delta I/I_0$ is proportional to $\mathrm{Re}[\Delta\xi(\tau)]$ only. Therefore, for a convenient choice of the couple (θ,ϕ), it is possible to measure independently the pump-induced modification to either the real or imaginary parts of the complex reflection coefficient of the sample.

4. Application to the interferometric detection of ultrafast acoustic waves

We illustrate the performances of the interferometer by investigating the opto-acoustic response up to 100 GHz of a submicronic tungsten layer deposited on top of a (100)-silicon substrate. Following the absorption of the pump pulse, the sudden thermal stress created in the sample generates high frequency acoustic waves in the GHz to THz range. These waves are detected through the transient perturbation of the optical reflection coefficient r_0 of the sample [21]. Except in specific cases [32–37], measurements sensitive to the intensity of the probe pulse bring information on the real part of the transient reflectivity [21] through photo-elastic coupling. On the other hand, interferometric measurements allow resolving both the real and imaginary parts of the transient reflectivity [10, 12, 38]. The imaginary part is mainly sensitive to the displacement of interfaces in the sample. As explained in the previous sections, the interferometer presented here gives access to the temporal derivative of the perturbation, i.e. to the measurement either of the temporal derivative of the photo-elastic contribution (real part), or of the out-of-plane surface velocity of interfaces in the sample (imaginary part) [39, 40].

We first present the transient dynamics of the thin tungsten film detected by a direct measurement of the intensity of the probe pulse. This experimental configuration is called reflectometry in the following and is presented in Fig. 3(a). For this purpose, the polarization of the incident pulse P_I on the calcite crystal is set at 0°. Thus, a single probe pulse is focused on the tungsten film. The resulting dynamics with respect to the pump-probe delay τ is plotted in Fig. 3(b) (dashed curve). The energy of the pump and probe pulses at the sample position are 1 nJ and 0.5 nJ, respectively. The sharp peak at $\tau = 0$ is the signature of the almost instantaneous electronic response of tungsten [41]. Over the slow decaying thermal background after $\tau = 0$, the acoustic echoes are detected periodically at the free surface of the film every ≈ 100 ps. They are the hallmark of the longitudinal acoustic wave bouncing back and forth in the thin film. The dashed curve in the inset of Fig. 3(b) shows the acoustic part of the reflectometric signal after subtraction of the thermal background. These echoes are detected by the single probe pulse through the photoelastic interaction over the optical penetration depth in tungsten. The temporal shape of the echoes is closely related to the strain profile inside the film [21].

The opto-acoustic response of the thin film is now investigated with the common-path interferometer described in the previous sections [Fig. 3(a)]. For this purpose, the polarization of the incident pulse P_I on the calcite crystal is turned to -45 degrees. Measurements presented in Fig. 3(b) have been performed close to the dark fringe located at $(\theta,\phi) = (3\pi/4, 3\pi/4)$. Accordingly with the analysis built in section 3 (cf Fig. 2) , we choose $\delta\theta = 4°$ and $\delta\phi = 4°$ to measure the temporal derivative of the real part of the transient reflectivity (grey continuous curve) and $\delta\phi = 0°$ and $\delta\theta = 2°$ to measure the temporal derivative of the imaginary part of the transient reflectivity (black continuous curve). As for measurements in reflectometry, an almost instantaneous electronic response followed by acoustic echoes over a thermal diffusion

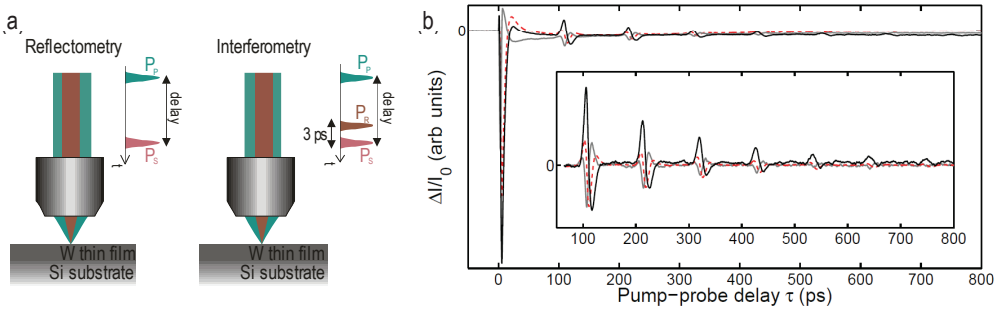

Fig. 3. (a) Experimental configurations for measurements in reflectometry or interferometry. (b) Experimental measurement in reflectometry (dashed curve) and in interferometry (continuous curves) of the transient optical response of the thin film. For measurements in interferometry, both the real part (gray continuous curve) and the imaginary part (black continuous curve) of the temporal derivative of the complex perturbed optical reflection coefficient are displayed. For the three signals, an almost instantaneous electronic response is followed by periodic acoustic echoes over a thermal diffusion background. The inset shows the acoustic part of the signals after subtraction of the thermal diffusion background.

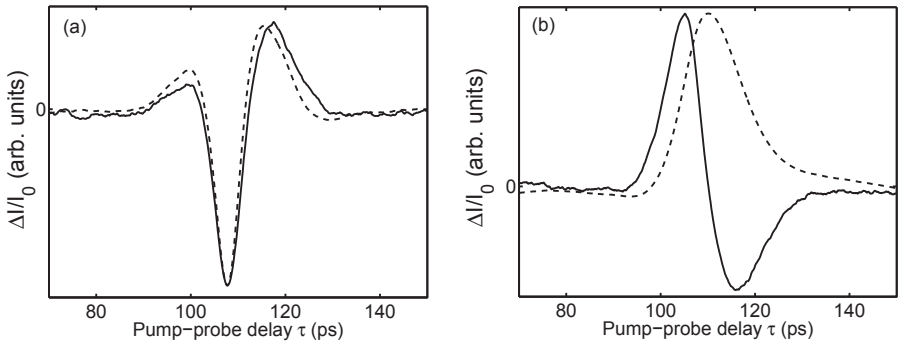

Fig. 4. Magnification on the first acoustic echoe shown in the inset of Fig. 3(b). (a) Real part of the interferometric signal (continuous curve) and numerical derivation of the first acoustic echo detected in reflectometry (dashed curve). (b) Imaginary part of the interferometric signal (continuous curve) revealing the out-of-plane surface velocity. Integration over time of the imaginary part (dashed curve) shows monopolar surface displacement (in agreement with predictions).

background are observed. The inset in Fig. 3(b) shows the acoustic part of the signals after subtraction of the thermal component. To allow a direct comparison of the transient dynamics measured in reflectometry and in interferometry, Fig. 3(b) is presented in arbitrary units. However, it is worth noting that the lowest value of $\Delta I/I_0$ detectable with this interferometer is of the order of 10^{-6}.

To analyze in more details the temporal shape of the echoes measured in interferometry, a magnification on the first acoustic echo is shown in Fig. 4. The real part of the interferometric signal corresponds to the continuous curve in Fig. 4(a) while the dashed curve results from the numerical derivation of the first acoustic echo detected in reflectometry. The two curves have been normalized for the purpose of comparison. The very good agreement between the two curves confirms that the interferometer is sensitive to the derivative of the reflectometric signal along the working line $\delta\theta = \delta\phi$ (cf Fig. 2). On the other hand, the continuous curve in Fig. 4(b) represents the imaginary part of the interferometric signal, while the dashed curve corresponds to its numerical integration over time. The bipolar signature of the detected out-of-plane surface velocity (continuous curve) is perfectly consistent with the monopolar signature of the displacement field, as expected at the free surface of the film (dashed curve) [42].

5. Conclusion

We have presented an in-line femtosecond common-path interferometer suited for experiments in reflection mode. A single birefringent crystal is used first to generate a pair of phase-locked pulses and second to recombine them and build interferences. The alignment of the interferometer is straightforward since probe and reference arms are spatially overlapped all along the optical path. Furthermore, this very compact interferometer is fully passive: No mechanical or thermal active stabilization is necessary. The analytical modeling developed in the framework of the Jones formalism has shown that the temporal derivative of the real or imaginary parts of the complex perturbed optical reflection coefficient can be measured independently. We have demonstrated the ability of the interferometer to be sensitive either to the acousto-optic interaction or to the ultrafast surface displacements have been demonstrated. These results are illustrative of the performances of the interferometer. Furthermore, the sensitivity to the ultrafast changes of the complex optical index will also allow to investigate semi-conductors or dielectric. The range of application of this interferometer will thus span the broader domain of laser-matter interaction.

Acknowledgments

This work has been financially supported by the Agence Nationale de la Recherche (project NanoVibe ANR-11JS09-013-01, project picoBond ANR-13-BS09-0021-01, project PHEMTO), the competitiveness cluster Route des Lasers, the Région Aquitaine (project 2012-16-03-011), the University of Bordeaux and Bordeaux INP.